



Research paper

Fabrication of two lanthanides co-doped Bi₂MoO₆ photocatalyst: Selection, design and mechanism of Ln₁/Ln₂ redox couple for enhancing photocatalytic activity



Hongda Li, Wenjun Li*, Fangzhi Wang, Xintong Liu, Chaojun Ren

Beijing Key Laboratory for Science and Application of Functional Molecular and Crystalline Materials, University of Science and Technology Beijing, Beijing 100083, China

ARTICLE INFO

Article history:

Received 3 March 2017

Received in revised form 2 June 2017

Accepted 5 June 2017

Available online 10 June 2017

Keywords:

Ln₁/Ln₂ co-doped bismuth molybdate

Photocatalysts

Redox couple

ABSTRACT

Various Ln_a/Ln_b co-doped bismuth molybdate (Bi₂MoO₆) photocatalysts were synthesized by a hydrothermal process. The result of photocatalytic experiment demonstrated that the relevant Ln₁³⁺ 4f^{7+x}/Ln₂³⁺ 4f^{7-x} (Ln₁/Ln₂ = Tb/Eu, Dy/Sm, Er/Nd; x = 1, 2, 4) co-doped Bi₂MoO₆ samples shows higher photocatalytic activities. Moreover, all the photocatalytic activities of Ln₁/Ln₂ co-doped Bi₂MoO₆ were higher than that of the corresponding single-doped Bi₂MoO₆. The crystalline structures, morphology, constituent contents, chemical state and optical properties of the samples were analyzed in detail. Meanwhile, a new conjecture about the complementary distribution of 4f orbital electrons in the Ln₁/Ln₂ redox couple was proposed through co-doping with Ln₁ and Ln₂ ions to improve the photocatalytic activity of Bi₂MoO₆. For the Bi₂MoO₆ photocatalyst, Dy/Sm co-doping displayed the strongest photocurrent response as well as the best photocatalytic activity, while Tb/Eu co-doping displayed the apparently extended visible-light absorption region. These findings provides a novel strategy to fabricate and engineer high-efficiency photocatalysts by selecting appropriate Ln₁/Ln₂ redox couple.

© 2017 Elsevier B.V. All rights reserved.

1. Introduction

Semiconductor photocatalysis technology has the potential to be a beneficial and green technology for improving environmental and energy concerns [1–3]. Almost all of the traditional single-component photocatalysts have intrinsic drawbacks, which greatly limit their practical application. Some common drawbacks of these photocatalysts include limited light absorption and rapid recombination of photo-induced charge carriers. In order to solve these problems, designing and synthesizing a modified material by doping with metal, non-metal ions or ionic group [4–6]; building heterojunction photocatalysts [7,8]; and loading noble metal cocatalysts [9,10] have become the widely used research methods. Results from these modified materials indicate that the recombination of electron-hole can be availably restrained, and the light absorption can be extended to longer wavelengths, which leads to a high photocatalytic activity.

As a kind of simple and controllable modification method, doping is a fundamental strategy to introduce dopants into a crystal structure, which can mediate the properties of photocatalysts. Generally, introducing dopants to improve the activity of photocatalysts often exhibit two kinds of approaches. One is focused on the extension of photo-response region by introducing doping level such as N-doped TiO₂/C, S-doped g-C₃N₄ and metal-doped TiO₂ [11–13]; as well as up-converting visible light into ultraviolet light, just like Er-doped BiVO₄ [14]. The second approach is concentrated on promoting the separation of photo-generated electron-hole pairs by fabricating crystal defects [15,16] or building redox centers in the crystal structure, such as Tb-doped Bi₂MoO₆ and Ce-doped Bi₂MoO₆ [17,18]. Additionally, recent studies reported that the more effective photocatalysts can be received by co-doping with two dopant element (e.g., Sm/N co-doped Bi₂WO₆, Cu/N co-doped TiO₂, and Fe/Eu co-doped TiO₂) [19–21], which does not only result in a synergic effect to improve the visible-light absorption efficiency of photocatalysts, but also restrain the recombination rate of the photo-induced carriers.

Particularly, the lanthanide ions are regarded as the ideal metal-dopants to enhance the photocatalytic activities of catalysts because of their unique optical properties and 4f electron configu-

* Corresponding author.

E-mail address: wjli_ustb@163.com (W. Li).

ration. Recently, there are a few reports about co-doping with two kinds of lanthanide elements to obtain high-efficiency photocatalysts. The studies demonstrated that co-doping of two lanthanide elements in photocatalysts can either convert low-energy light to higher-energy light via multiple absorption and energy transfer [22–24], or facilitate charge separation and restrain recombination via the formed redox cycles [25] to achieve higher photocatalytic performance. The co-doped photocatalysts displayed a much higher photocatalytic activity than that of the single or non-doped samples. However, there are more than a dozen lanthanide elements, and the study on how to select the appropriate dopants of lanthanide-ions pair to achieve a high-efficiency photocatalyst has not been reported. Furthermore, the study of co-doping with two lanthanide elements in photocatalyst is just at its beginning, and the details of the mechanism of a synergistic effect between two lanthanide elements are still not entirely understood. More in-depth work for this issue is needed.

Gd³⁺ ions doped photocatalyst has the best photocatalytic activity in comparison to the other single lanthanide-doped catalysts [26,27], because of its half-filled 4f orbital that holds 7 f-electrons; this configuration is relatively stable [28,29]. According to the configuration of Gd³⁺ 4f orbital, gadolinium is regarded as symmetric center and two kinds of lanthanide ions, whose average number of 4f electrons is seven, are selected as co-doping ions. It might be possible to select and engineer the appropriate lanthanide ions pairs co-doping to mediate the photocatalytic activity; the higher-efficiency photocatalysts could be achieved by using this approach, which attributes to a synergistic effect between two kinds of lanthanide ions instead of the single effect of Gd³⁺ ions.

Bismuth molybdate (Bi₂MoO₆) belongs to the Aurillius family has attracted significant attention because of its luminescent, dielectric and photocatalytic properties [30–32]. However, the visible-light-responsive photocatalytic application of Bi₂MoO₆ is limited by its rapid electron–hole recombination and lower visible-light absorption efficiency. In this study, various Ln_a/Ln_b co-doped Bi₂MoO₆ photocatalysts were synthesized by a hydrothermal process, and the relevant Ln₁³⁺ 4f^{7+x}/Ln₂³⁺ 4f^{7-x} (Ln₁/Ln₂ = Tb/Eu, Dy/Sm, Er/Nd; x = 1, 2, 4) co-doped Bi₂MoO₆ samples shows higher photocatalytic activities. Meanwhile, a new conjecture about the complementary distribution of 4f orbital electrons in the Ln₁/Ln₂ redox couple was proposed to discuss the synergistic effect between two lanthanide ions. What's more, the different properties in charge carriers separation and light absorption were attributed to the various Ln₁/Ln₂ co-doping in photocatalysts, thereby achieving different photocatalytic activities. According to the nature of photocatalysts, the heterodinuclear redox couple engineering provides a novel strategy to fabricate high-efficiency photocatalysts by selecting the appropriate Ln₁/Ln₂ redox couple.

2. Experimental section

2.1. Synthesis of the photocatalysts

The Ln-doped Bi₂MoO₆ (Ln-BMO, Ln = Nd, Sm, Eu, Gd, Tb, Dy, and Er), Ln₁/Ln₂ co-doped Bi₂MoO₆ (Ln₁/Ln₂-BMO, Ln₁/Ln₂ = Tb/Eu, Dy/Sm, and Er/Nd) and Ln_a/Ln_b co-doped Bi₂MoO₆ (Ln_a/Ln_b-BMO, Ln_a/Ln_b = Tb/Dy, Tb/Er, Tb/Sm, Tb/Nd, Dy/Er, Dy/Eu, Dy/Nd, Er/Eu and Er/Sm) samples were synthesized by a hydrothermal method: 0.970 g (2 mmol) of Bi(NO₃)₃•5H₂O and 0.176 g (0.14 mmol) of (NH₄)₆Mo₇O₂₄•4H₂O were respectively dissolved in 40 mL nitric acid solution (2 mol L⁻¹) and 40 mL deionized water to form the transparent solutions. Then, the (NH₄)₆Mo₇O₂₄ solution was added dropwise into the Bi(NO₃)₃ solution and stirred for 0.5 h. Afterwards, a certain amount of Ln(NO₃)₃ solutions were respectively dropwise added into the mixed solutions and dilute ammonia solu-

tion was employed to ensure the pH values of the systems to be ca. 9. After stirring for 20 min, the mixtures were then transferred to the 100 mL Teflon-lined stainless steel autoclave and maintained at 180 °C for 12 h. At last, the products were collected by filtration then washed with deionized water four times and dried at 80 °C for 8 h. The as-prepared samples were as follows: 2% Gd-BMO, 3% Tb-BMO, 3% Tb/1% Eu-BMO, 3% Tb/3% Eu-BMO (Tb/Eu-BMO), 3% Tb/5% Eu-BMO, 3% Eu-BMO, 3% Dy-BMO, 3% Dy/1% Sm-BMO, 3% Dy/3% Sm-BMO (Dy/Sm-BMO), 3% Dy/5% Sm-BMO, 3% Sm-BMO, 2% Er-BMO, 2% Er/1% Nd-BMO, 2% Er/2% Nd-BMO (Er/Nd-BMO), 2% Er/3% Nd-BMO, 2% Nd-BMO, 3% Tb/3% Dy-BMO, 3% Tb/1% Er-BMO, 3% Tb/1% Sm-BMO, 3% Tb/1% Nd-BMO, 3% Dy/1% Er-BMO, 3% Dy/1% Eu-BMO, 3% Dy/1% Nd-BMO, 2% Er/1% Eu-BMO and 2% Er/1% Sm-BMO. All the percentage are the atomic ratio of Ln/Bi.

2.2. Characterization

The crystalline phases of the as-prepared samples were collected by powder X-ray diffraction (XRD) (D/MAX-RB, Rigaku, Japan) with a Cu K α radiation of $\lambda = 0.15405$. Raman spectra were recorded by Raman spectrometer (T64000, Horiba LabRam, France) at 532 nm excitation wavelengths. The morphology differences and element mapping images of the samples were measured by a scanning electron microscope (SEM) (SU8010, Hitachi, Japan) at accelerating voltage of 15.0 kV and a transmission electron microscope (TEM) (F-20, FEI, USA) operated at 200 kV. X-ray photoelectron spectra (XPS) were measured by an ESCALAB 250Xi photoelectron spectrometer by using Al K α radiation as the source. The specific surface areas of the samples were collected by the Brunauer–Emmett–Teller (BET) method (NOVA 4200e, Quantachrome, USA). The UV–vis diffuse reflectance spectra (DRS) of obtained samples were collected on an UV–vis spectrophotometer (T9s, Persee, China) with BaSO₄ as a reference.

2.3. Photocatalytic experiment

The photocatalytic performance of obtained samples were evaluated by degrading 12 mg L⁻¹ rhodamine B (RhB) and 15 mg L⁻¹ phenol under a source of 400 W Xe lamp irradiation with a UV-cutoff filter ($\lambda > 420$ nm). In each experiment, powder photocatalyst (40 mg) was dispersed in 40 mL of organics solution with vigorous stirring. Before light irradiation, the suspensions were vigorously stirred for 1 h to reach an adsorption–desorption equilibrium in the dark. During the photoreaction, the reaction photocatalysts were collected at 1 h intervals for organics degradation, and then centrifuged to remove the solid photocatalysts. The ratios (C/C₀) of the organics were employed to assess the degradation rate by detecting the absorbance spectra at 554 nm for RhB or 270 nm for phenol by a UV–vis spectrophotometer.

2.4. Photocurrent measurement

Photoelectrochemical measurements were obtained using an electrochemical workstation (5060F; RST, China) in a conventional three-electrode system with a 0.5 mol L⁻¹ Na₂SO₄ aqueous solution. The samples, a calomel electrode (saturated KCl), and a Pt wire were employed as the working electrode, reference electrode, and counter electrode, respectively. And a 0.5 mol L⁻¹ Na₂SO₄ aqueous solution was introduced as electrolyte. A 100 W incandescent lamp with a 420 nm cut off filter was used as the light source. The preparation of the working electrode is described below: 4 mg samples were dispersed in 1 mL of ethanol and Nafion solution (v/v = 30:1), followed by spreading on the bottom middle of an ITO glass in a circle with a diameter of 6 mm. Then the photocurrents of the photocatalysts with the light on and off were measured at 0.8 V.

3. Results and discussion

3.1. Structural analysis

X-ray diffraction patterns of the pure BMO and the doped BMO samples are shown in Fig. 1. All diffraction peaks could be indexed to a koechlinite Bi_2MoO_6 structure (JCPDS card no. 21-0102). As shown in Fig. 1a, the distinctive peaks at $2\theta = 28.2^\circ$, 32.5° , 32.6° , 33.1° , 46.7° , 47.1° , 55.5° , and 56.2° which were indexed to the (1 3 1), (2 0 0), (0 0 2), (0 6 0), (2 0 2), (2 6 0), (3 3 1) and (1 9 1) planes, respectively. Doping of a low-concentration lanthanide ions did not generate any crystalline phases of lanthanide species. In addition, some shifts of the peaks at 2θ values of 28.2 were observed, which corresponding to the (1 3 1) plane (Fig. 1b). The different lanthanide ions have different electronic structure and radius, which resulted in different bonding effect after the substitution of lanthanide ions by Bi in BMO crystal. Therefore, it can also result in different degree or direction of peaks shift after doping with different lanthanide ions [33,34]. It can be observed that doping of erbium (Er), europium (Eu) or dysprosium (Dy) results in different degree or direction of shift in the peak at 2θ values of 28.2, respectively, but no obvious shift after doping of terbium (Tb), samarium (Sm) or neodymium (Nd). Interestingly, an opposite direction of peak shift at $2\theta = 28.2^\circ$ occurred in Ln_1/Ln_2 co-doped BMO ($\text{Ln}_1/\text{Ln}_2 = \text{Tb}/\text{Eu}$, Dy/Sm , or Er/Nd) as comparison to that of Ln_1 or Ln_2 single-doped BMO, such as a left shift in Dy-BMO, no obvious shift in Sm-BMO, but a right shift in Dy/Sm-BMO. These results implied that there are some overlaps of the bonding effects between Ln_1 and Ln_2 in BMO crystal, which led to the opposite direction of peak shift between the effects of co-doping and single-doping for peak shift [35]. In other words, there are some interactions between Ln_1 and Ln_2 ions instead of an individual effect in BMO crystal.

3.2. Morphology and component characterization

Fig. 2 illustrates the SEM images of pure BMO and Ln_1/Ln_2 -BMO ($\text{Ln}_1/\text{Ln}_2 = \text{Tb}/\text{Eu}$, Dy/Sm , Er/Nd). All samples displayed a sheet-like morphology. As shown in Fig. 2a, pure BMO exhibited an irregular sheet-like microstructure and a smooth surface. The morphologies of Tb/Eu-BMO, Dy/Sm-BMO and Er/Nd-BMO (Fig. 2b–d) keep the sheet-like shapes and smooth surfaces as with pure BMO, which implied that Ln_1/Ln_2 ions co-doping have almost no effect on the morphology of BMO. The insets of Fig. 2b–d displayed the corresponding element mapping images of dopants, whereas bismuth, molybdate and oxygen were all homogeneous and was not exhibited here. It indicated a uniform distribution of the elements in the whole imaging area of the corresponding SEM images, reasonably implying that Ln_1/Ln_2 dissolved into the BMO substrate evenly [36]. In addition, real content of Ln_1/Ln_2 in the Ln_1/Ln_2 -BMO samples were calculated from energy-dispersion x-ray spectroscopy (EDS) data and were listed in Table 1. The result of EDS reveals that their atomic ratio of $\text{Ln}:\text{Bi}$ are all approximating the value of charging ratio, which indicated that almost all Ln_1/Ln_2 ions have been introduced into the lattice of BMO.

The high-resolution transmission electron microscopy (HRTEM) is a widely used characterization to investigate the microstructure of materials. Fig. 3 reveals the HRTEM images of pure BMO and Ln_1/Ln_2 -BMO ($\text{Ln}_1/\text{Ln}_2 = \text{Tb}/\text{Eu}$, Dy/Sm and Er/Nd). Fig. 3a shows that the interplanar spacing of 0.315 nm is well-matched with the (1 3 1) lattice plane of the koechlinite BMO. Interestingly, the interplanar spacings of 0.275 and 0.274 nm are observed by co-doping of Ln_1/Ln_2 in BMO, and they are well-matched with the (2 0 0) and (0 0 2) lattice planes of BMO, respectively, which indicated that all the Tb/Eu-BMO, Dy/Sm-BMO and Er/Nd-BMO nanosheets have a preferential {0 1 0} orientation. In addition, the results implied

that doping of a low-concentration lanthanide ions did not generate any other lanthanide species.

3.3. Chemical state analysis

The X-ray photoelectron spectroscopy (XPS) of the obtained photocatalysts can help us to investigate the chemical state and bonding situation of elements in pure BMO, Tb/Eu-BMO, Dy/Sm-BMO and Er/Nd-BMO. Before analysis, all the signals of detected elements were calibrated using the binding energy of C 1s at 284.8 eV before analysis. As shown in Fig. 4a, the overall XPS spectra of pure BMO, Tb/Eu-BMO, Dy/Sm-BMO and Er/Nd-BMO display the characteristic peaks of Bi, Mo, O, Tb, Eu, Dy, Sm, Er and Nd elements. The binding energies of O 1s in Tb/Eu-BMO (529.9 eV), Dy/Sm-BMO (530.3 eV) and Er/Nd-BMO (530.3 eV) apparently shift towards to higher binding energies in comparison with pure BMO (529.8 eV) as shown in Fig. 4b. These results can be attributable to the formation of Ln–O bonds which have higher binding energy of O 1s than Bi–O (529.4 eV), such as Tb–O bonds (529.5 eV) and Eu–O bonds (531.1 eV) in Tb/Eu-BMO, Dy–O bonds (531.9 eV) and Sm–O bonds (530.4 eV) in Dy/Sm-BMO, Er–O bonds (532.2 eV) and Nd–O bonds (532.4 eV) in Er/Nd-BMO, respectively [37–40]. Fig. 5c–h show the high-resolution XPS spectra of (c) Tb 3d and (d) Eu 3d for Tb/Eu-BMO, (e) Dy 3d and (f) Sm 3d for Dy/Sm-BMO, (g) Er 4d and (h) Nd 3d for Er/Nd-BMO, respectively. The XPS signals of Tb/Eu-BMO in Fig. 5c and 5d were specified as the Tb^{3+} $3d_{5/2}$ and $3d_{3/2}$ states at 1242.9 and 1276.2 eV, Eu^{3+} $3d_{5/2}$ and $3d_{3/2}$ states at 1133.7 and 1163.4 eV, respectively. The XPS signals of Dy/Sm-BMO in Fig. 5e and 5f were ascribed to the Dy^{3+} $3d_{5/2}$ and $3d_{3/2}$ states at 1303.6 and 1335.4 eV, Sm^{3+} $3d_{5/2}$ and $3d_{3/2}$ states at 1083.4 and 1110.8 eV, respectively. In the XPS signals of Er/Nd-BMO, the binding energy peak located at 169.9 eV corresponds well with the Er 4d of Er^{3+} (Fig. 4g). And the binding energy values of Nd $3d_{5/2}$ and $3d_{3/2}$ were observed at 973.6 & 982.8 eV and 994.1 & 1006.0 eV (Fig. 4h), respectively, which indicated that the Nd element in BMO was mainly +3 [41].

3.4. Optical property

UV–vis diffuse reflectance spectra (DRS) was employed to investigate the optical absorption properties of pure BMO and doped BMO (Fig. 5). Except for the Er-BMO sample, a different degree red-shift of the optical absorption edge was detected from the obtained samples compared with pure BMO. In addition, a new absorption band centered at ca. 523 nm was observed for the DRS of Er-BMO and Er/Nd-BMO, which could be assigned to the energy level transition of Er^{3+} [42]. Meanwhile, another new absorption band at ca. 587 nm for Nd-BMO and Er/Nd-BMO, which could be attributed to the energy level transition of Nd^{3+} [43]. The band gap energy (E_g) values of the semiconductor samples were calculated by using the equation $Ah\nu = \alpha(h\nu - E_g)^{n/2}$ [44], where α , h , ν , and E_g are the absorption coefficient, Planck's constant, light frequency, and band gap energy, respectively. Bi_2MoO_6 is a direct band gap semiconductor [45], thus $n = 1$. From the inset in Fig. 5, the band gaps of pure BMO, Tb-BMO, Eu-BMO, Tb/Eu-BMO, Dy-BMO, Sm-BMO, Dy/Sm-BMO, Er-BMO, Nd-BMO and Er/Nd-BMO were calculated to be approximately 2.58, 2.47, 2.51, 2.19, 2.47, 2.50, 2.48, 2.59, 2.49 and 2.47 eV, respectively. The results indicated that co-doping with two different lanthanide ions offers a synergetic effect for enhancing the visible-light absorption of BMO. Additionally, it can be found that the visible-light absorption region of BMO was apparently promoted by Tb/Eu (2.19 eV) co-doping much more than that of Dy/Sm (2.48 eV) and Er/Nd (2.47 eV) co-doping.

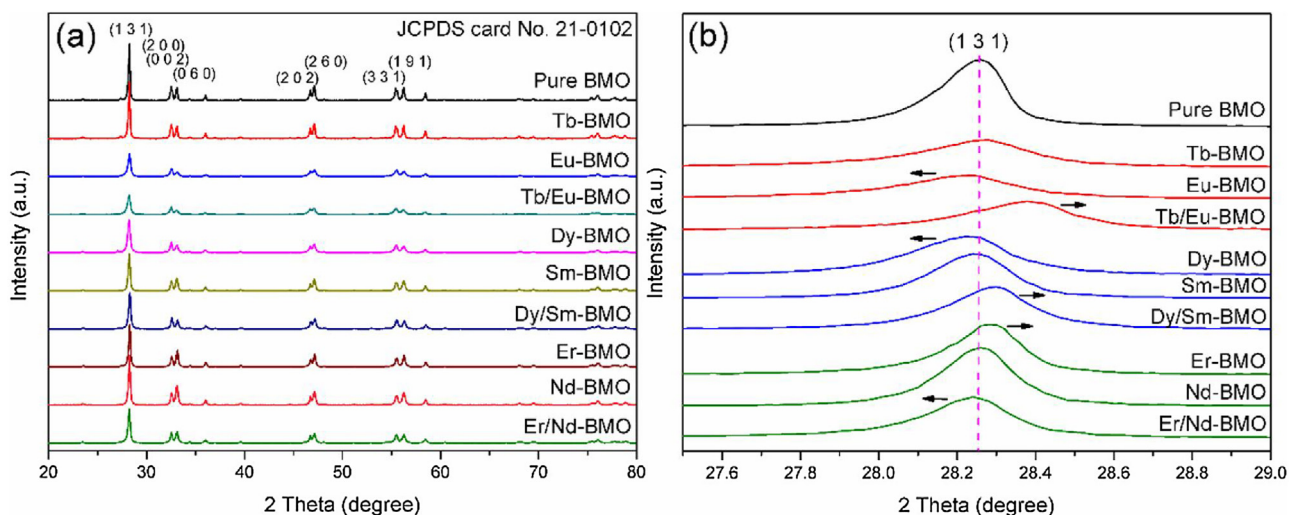


Fig. 1. (a) XRD patterns and (b) XRD peaks in the (1 3 1) plane of the pure BMO and lanthanide-doped series of BMO samples.

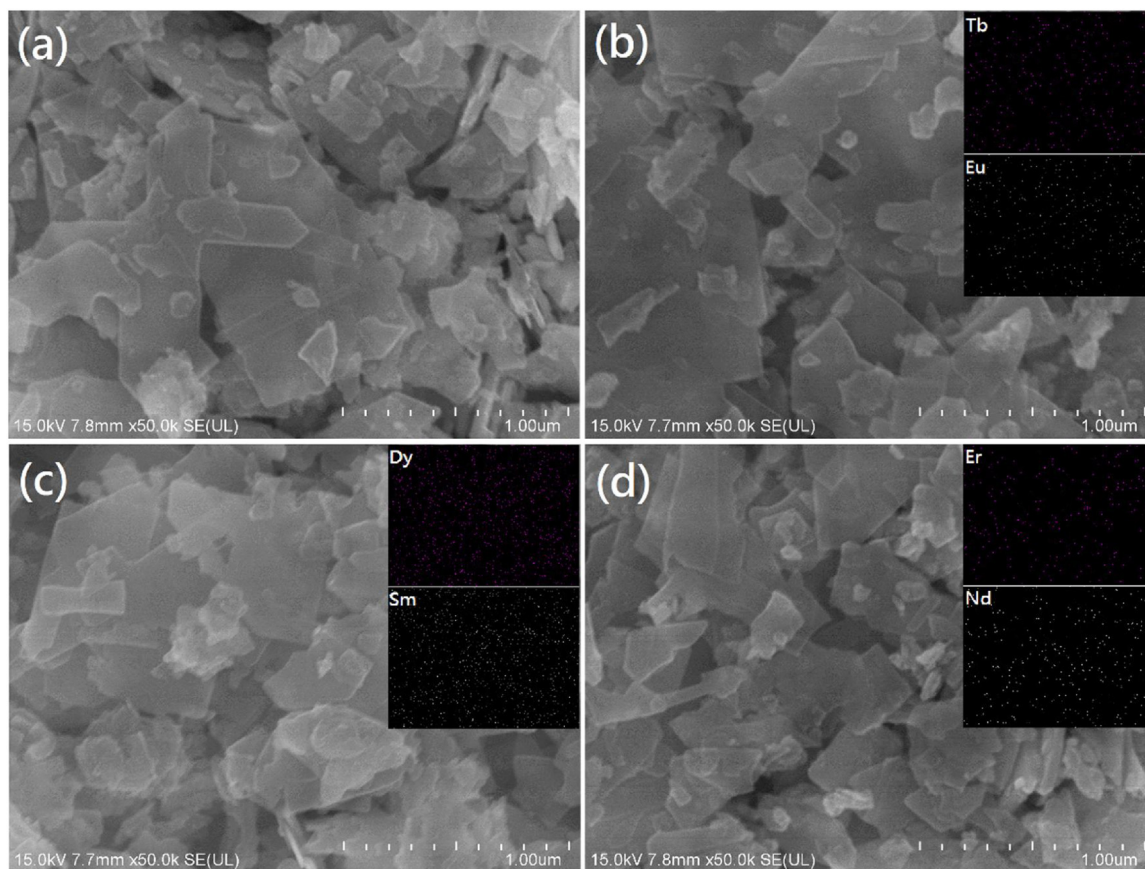


Fig. 2. SEM images of pure BMO, Tb/Eu-BMO, Dy/Sm-BMO and Er/Nd-BMO; the insets display the corresponding element mapping images of dopants.

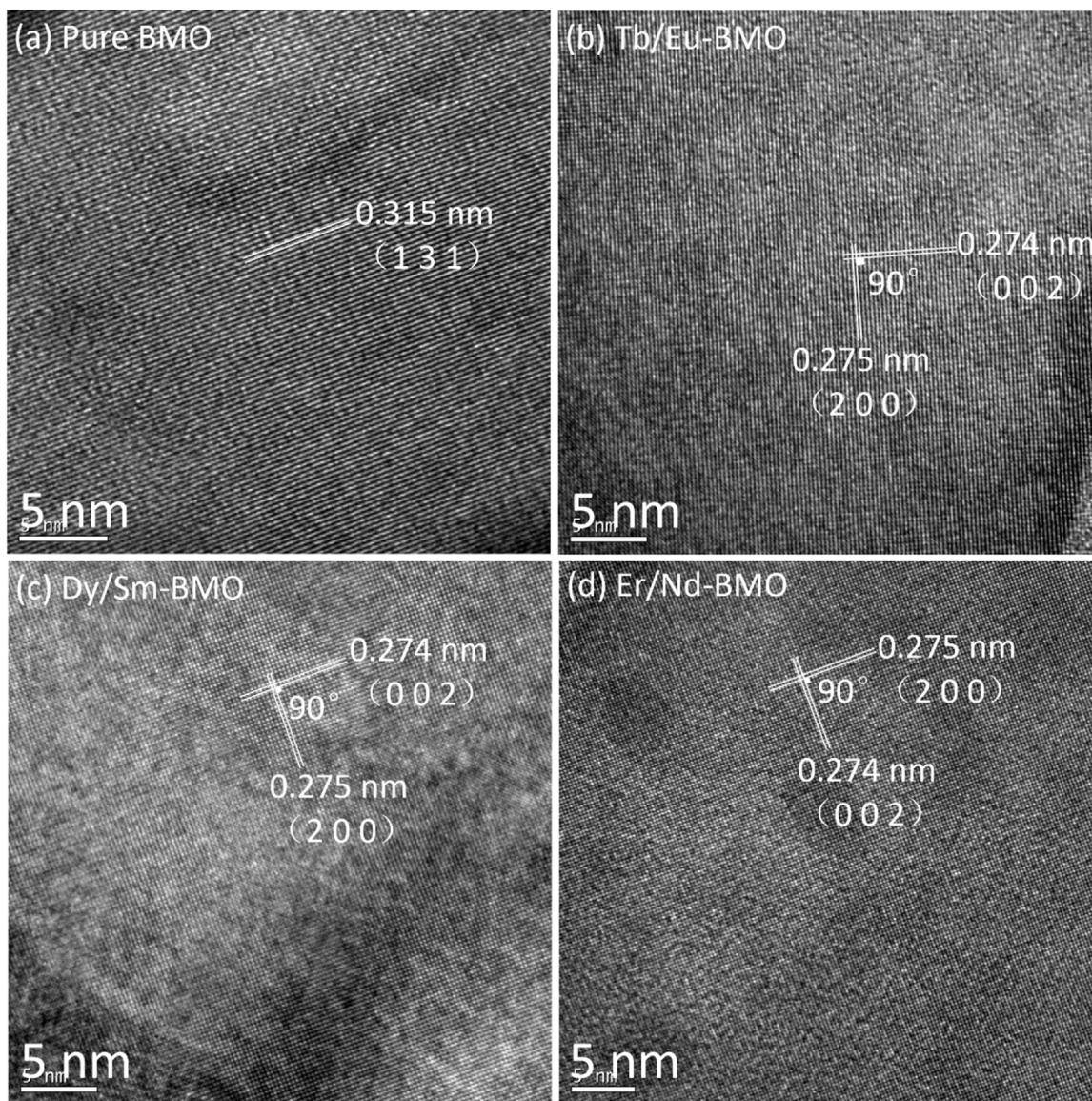
3.5. Photocatalytic property

Before analysis, and in the case of low concentration doping, all the photocatalytic activity of the single Ln-doped BMO (Ln = Tb, Eu, Dy, Sm, Er, Nd and Gd) samples have been evaluated by photodegrading RhB under visible light. The results indicated that the 3% Tb-BMO [18], 3% Dy-BMO [46], 2% Er-BMO [47] and 2% Gd-BMO [48] samples exhibited the highest photocatalytic activities compared with the corresponding lanthanide-doped BMO and pure BMO samples, respectively, while no available improved

effect for Eu-BMO, Sm-BMO and Nd-BMO. Moreover, the 2% Gd-BMO sample displayed the most improved photocatalytic performance. Herein, the photocatalytic activities of the pure and doped BMO photocatalysts were also evaluated by the photodegradation of RhB (12 mg L^{-1}) in aqueous solution under visible light (Fig. 6). Before irradiation, all photocatalysts were dispersed in RhB solution followed by stirring for 1 h in the dark to reach an adsorption-desorption equilibrium. It can be found from Fig. 6a that both 3% Tb/1% Eu-BMO and 3% Tb/3% Eu-BMO revealed apparently enhanced photocatalytic activity in comparison with pure

Table 1Real content of Ln_1/Ln_2 in the samples of $\text{Ln}_1/\text{Ln}_2\text{-BMO}$ ($\text{Ln}_1/\text{Ln}_2 = \text{Tb}/\text{Eu}$, Dy/Sm , and Er/Nd) from EDS data.

Sample	Element	Charging ratioAt% (Ln/Bi)	Real ratio		
			Wt%	At%	At% (Ln/Bi)
Tb/Eu-BMO	Bi		67.58	23.87	
	Tb	3	1.70	0.79	3.31
	Eu	3	1.46	0.71	2.97
Dy/Sm-BMO	Bi		68.15	24.59	
	Dy	3	1.56	0.72	2.93
	Sm	3	1.64	0.82	3.33
Er/Nd-BMO	Bi		67.36	23.56	
	Er	2	1.23	0.54	2.29
	Nd	2	0.79	0.40	1.70

**Fig. 3.** HRTEM images of (a) pure BMO, (b) Tb/Eu-BMO, (c) Dy/Sm-BMO and (d) Er/Nd-BMO.

BMO and single doped BMO, and 3% Tb/3% Eu-BMO (Tb/Eu-BMO) exhibited the most improved photocatalytic activity. The similar results as shown in Fig. 6b and c were observed that both 3% Dy/3% Sm-BMO (Dy/Sm-BMO) and 2% Er/2% Nd-BMO (Er/Nd-BMO) displayed the best photodegradation activity, respectively. For all the three kinds of ions pairs co-doped BMO, it can be found that the same proportion of Ln_1 and Ln_2 co-doped BMO displayed the

highest photocatalytic activity compared with that of the other corresponding samples, respectively. The results implied that certain positive synergistic effect were formed between the Ln_1 and Ln_2 ions, and the negative effect for the photocatalytic activities would be appeared if one of the ions doping was surplus or too few.

Besides the above three ions pairs, more ions pairs among the six elements (Nd, Sm, Eu, Tb, Dy and Er) were employed to co-

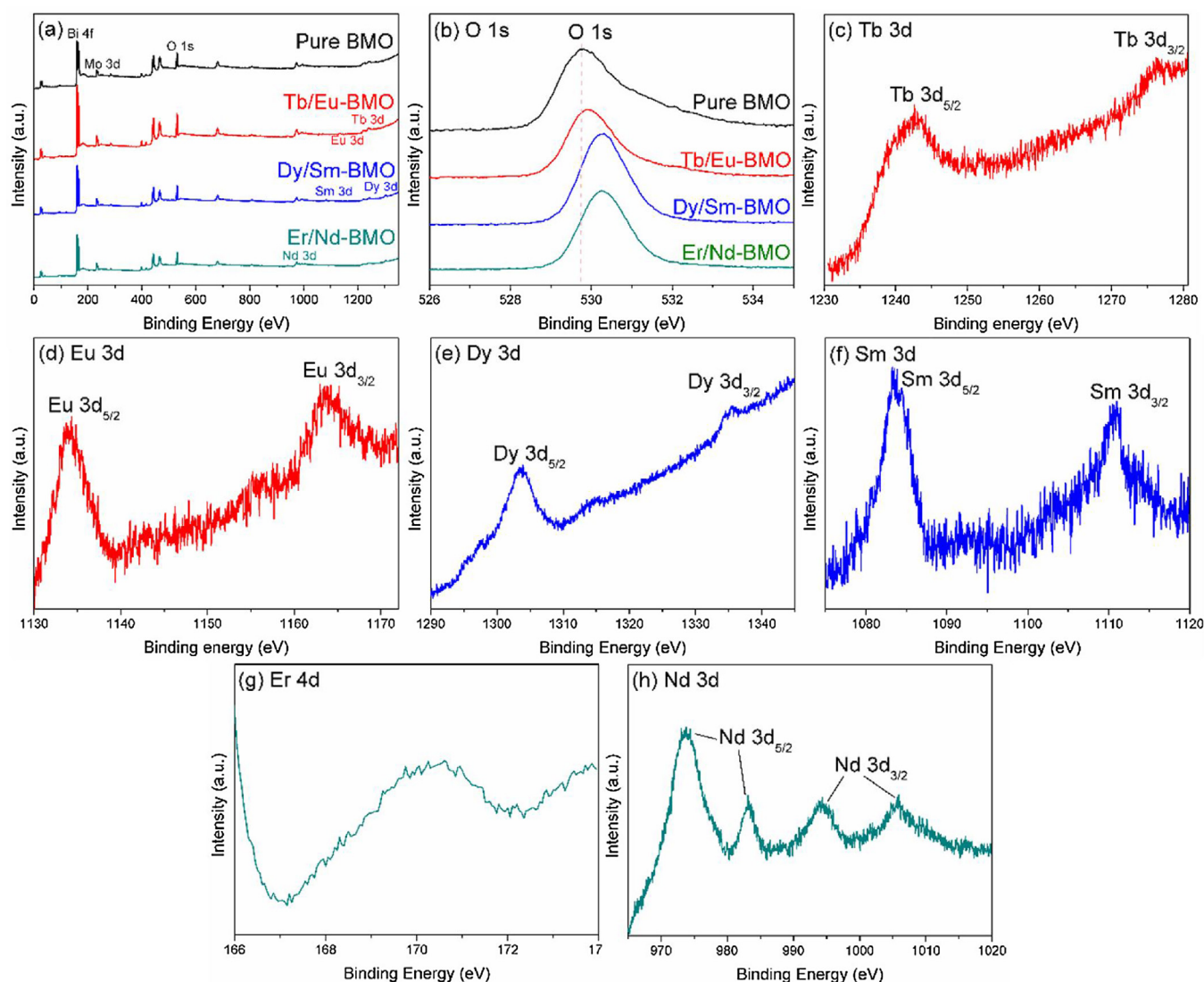


Fig. 4. (a) Overall XPS spectra of pure BMO, Tb/Eu-BMO, Dy/Sm-BMO and Er/Nd-BMO; (b) XPS analysis of O 1s in pure BMO, Tb/Eu-BMO, Dy/Sm-BMO and Er/Nd-BMO; XPS analysis of (c) Tb 3d and (d) Eu 3d in Tb/Eu-BMO, (e) Dy 3d and (f) Sm 3d in Dy/Sm-BMO, (g) Er 4d and (h) Nd 3d in Er/Nd-BMO, respectively.

Table 2

The concentration ratio of Tb/Dy, Tb/Er, Tb/Sm, Tb/Nd, Dy/Er, Dy/Eu, Dy/Nd, Er/Eu and Er/Sm and their degradation rates of RhB (40 mL, 12 mg L⁻¹) after 4 h of visible light irradiation.

Ln _a /Ln _b	Tb/Dy	Tb/Er	Tb/Sm	Tb/Nd	Dy/Er	Dy/Eu	Dy/Nd	Er/Eu	Er/Sm
Concentration ratio/at.%	3:3	3:1	3:1	3:1	3:3	3:1	3:1	2:1	2:1
Degradation rate/%	89.5	80.3	75.0	78.4	88.2	60.3	84.7	62.1	60.6

dope BMO, such as Tb/Dy, Tb/Er, Tb/Sm, Tb/Nd, Dy/Er, Dy/Eu, Dy/Nd, Er/Eu and Er/Sm. The best co-doping proportion in every ions pairs co-doping and their degradation rates of RhB after 4 h of visible light irradiation are list in Table 2. It was clear that all the photocatalytic activities of nine ions pairs co-doping were worse than that of Tb/Eu (95.9%), Dy/Sm (98.5%) and Er/Nd (91.6%) co-doping. In addition, there are no any rules in ions pairs selecting and co-doping proportion among nine ions pairs. These results demonstrated that the selected Ln₁/Ln₂ ions pairs (Ln₁/Ln₂ = Tb/Eu, Dy/Sm and Er/Nd) co-doping were the preferred plan within a certain scope.

As shown in Fig. 6d, the photocatalytic performance of pure BMO, Gd-BMO, Tb/Eu-BMO, Dy/Sm-BMO and Er/Nd-BMO were employed to make a detailed comparison. Before irradiation, the adsorption ratios of the previous five samples were collected after the adsorption-desorption equilibriums were achieved. All the five

samples presented almost the same capacity for RhB adsorption followed by 10.88%, 11.13%, 10.96%, 12.05% and 11.69%, because they had the similar surface areas, in order, were 13.86, 13.99, 14.38, 14.24 and 14.02 m² g⁻¹. It implied that the surface areas of sample is not the crucial factors of photocatalytic activity in this study. After 4 h of visible light irradiation, all the photodegradation rates of RhB for Tb/Eu-BMO (95.9%), Dy/Sm-BMO (98.5%) and Er/Nd-BMO (91.6%) were higher than that of pure BMO (48.9%) and 2% Gd-BMO (89.2%). The kinetics of the RhB decomposition over corresponding samples by employing a pseudo-first-order reaction kinetic model to fit the degradation data by the equation: $\ln(C_0/C) = kt + a$, where k is the apparent reaction rate constant. Fig. 6e shows the k (reaction rate constants) of the corresponding samples for the degradation of RhB. The corresponding k values were calculated to be 0.167 h⁻¹, 0.563 h⁻¹, 0.805 h⁻¹, 0.931 h⁻¹ and 0.626 h⁻¹ for pure BMO, Gd-

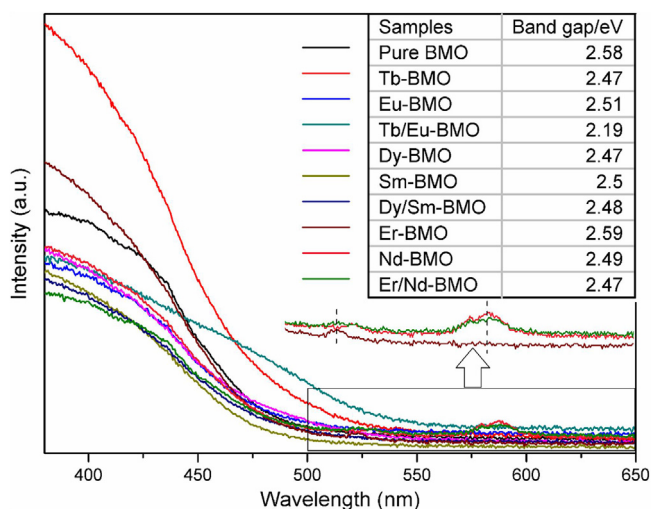


Fig. 5. The UV-vis diffuse reflectance spectra of the pure BMO, Tb-BMO, Eu-BMO, Tb/Eu-BMO, Dy-BMO, Sm-BMO, Dy/Sm-BMO, Er-BMO, Nd-BMO and Er/Nd-BMO samples; the inset displays the band gap energy of the corresponding samples.

BMO, Tb/Eu-BMO, Dy/Sm-BMO and Er/Nd-BMO, respectively. It is clear that the Dy/Sm-BMO sample displayed the best photocatalytic activity, which was approximately 4.8 times in comparison with that of pure BMO. This finding implied that co-doping with Ln_1 and Ln_2 in BMO ($\text{Ln}_1/\text{Ln}_2 = \text{Tb}/\text{Eu}$, Dy/Sm and Er/Nd) was beneficial to enhance their photocatalytic activity, which attributed to the synergetic effect between Ln_1 and Ln_2 .

Fig. 6f shows that the circulating experiment runs in the photodegradation of RhB were performed to verify the stability of the high-efficiency samples (Tb/Eu-BMO, Dy/Sm-BMO and Er/Nd-BMO) under visible light. The samples didn't exhibit any observable

loss of photocatalytic activities. It can be confirmed that the Ln_1/Ln_2 co-doped Bi_2MoO_6 photocatalysts aren't photo-corroded in the process of photodegrading RhB, which was specifically significant for their application.

Phenol presented characteristic absorption at the wavelength of 270 nm [49]. Fig. 7 shows the photocatalytic activities of the pure BMO and Ln_1/Ln_2 -BMO samples, which were evaluated by examining the photodegradation of phenol (15 mg L^{-1}) under 5 h of visible light irradiation. It can be observed that about 22.4% of phenol has been degraded over the pure BMO sample upon irradiation for 5 h. This percentage was even increased to 76.2%, 79.1% and 70.7% over the Tb/Eu-BMO, Dy/Sm-BMO and Er/Nd-BMO samples, respectively. Especially, Dy/Sm-BMO shows the highest photocatalytic activity for phenol which was about 2.5 times higher compared to that of pure BMO. The result further confirmed that co-doping with Ln_1/Ln_2 ions are positively contributed to enhance the photocatalytic activity of BMO.

3.6. Photocatalytic mechanism of Ln_1/Ln_2 -BMO

Overall, the visible-light photocatalytic activity of BMO was observably improved by co-doping with two specific lanthanide ions. Among these three Ln_1/Ln_2 ions pairs ($\text{Ln}_1/\text{Ln}_2 = \text{Tb}/\text{Eu}$, Dy/Sm and Er/Nd), a preliminary exploration in the mechanism of co-doping with terbium and europium in BMO has been proposed, which indicated that the formation of in-built Tb/Eu ions pairs that act as redox cycles to facilitate charge separation [25]. However, the detailed synergistic effect between terbium and europium ions has not yet been entirely understood, and also some of regulations need to explore that existed in co-doping with these ion pairs where located in the specific position of lanthanide elements. To study these, the photocurrent experiment was employed to explore the generation and transfer of photo-generated electron-holes pairs during the process of photocatalysis [50]. Fig. 8 reveals

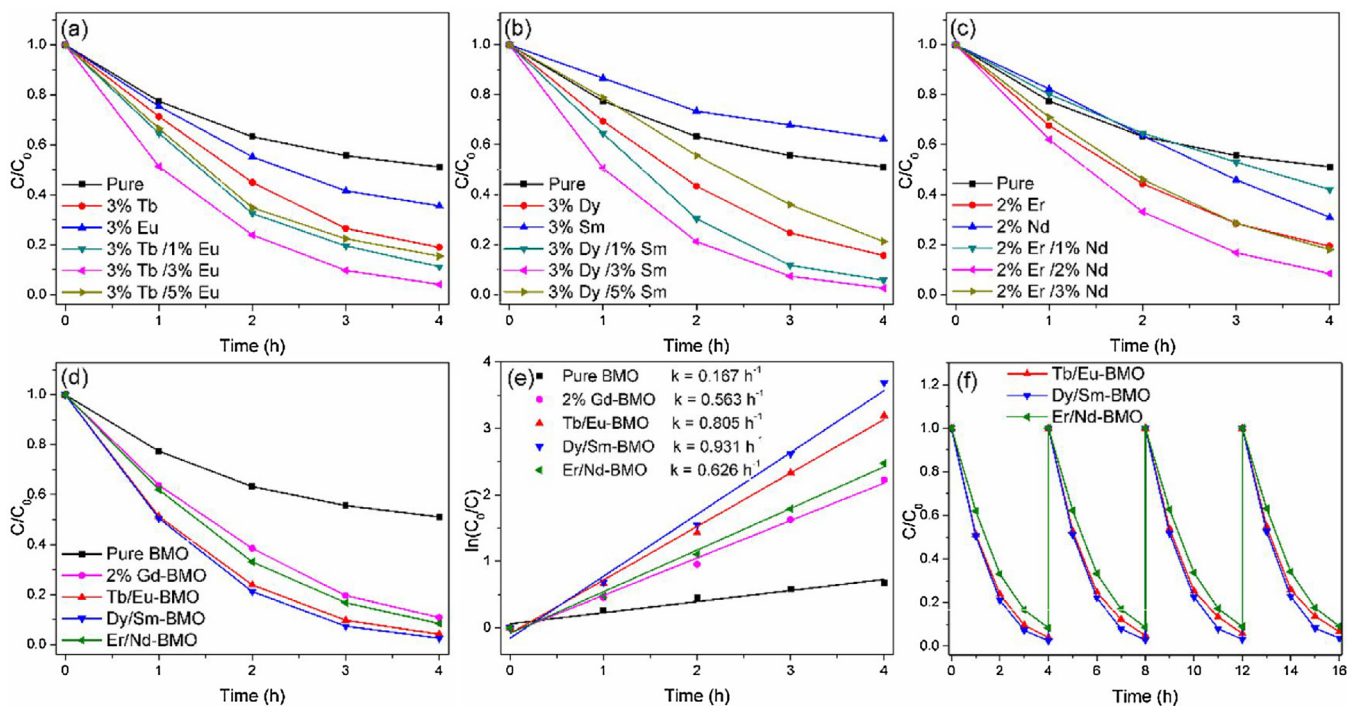


Fig. 6. Photocatalytic activity of RhB with (a) pure BMO, 3% Tb-BMO, 3% Eu-BMO, 3% Tb/1% Eu-BMO, 3% Tb/3% Eu-BMO and 3% Tb/5% Eu-BMO; (b) pure BMO, 3% Dy-BMO, 3% Sm-BMO, 3% Dy/1% Sm-BMO, 3% Dy/3% Sm-BMO and 3% Dy/5% Sm-BMO; (c) pure BMO, 2% Er-BMO, 2% Nd-BMO, 2% Er/1% Nd-BMO, 2% Er/2% Nd-BMO and 2% Er/3% Nd-BMO; (d) pure BMO, 2% Gd-BMO, 3% Tb/3% Eu-BMO (Tb/Eu-BMO), 3% Dy/3% Sm-BMO (Dy/Sm-BMO) and 2% Er/2% Nd-BMO (Er/Nd-BMO) under visible light irradiation; (e) Kinetics of RhB degradation over pure BMO, 2% Gd-BMO, Tb/BMO, Dy/Sm-BMO and Er/Nd-BMO; (f) Circulating experiment runs in the photodegradation of RhB over the Tb/Eu-BMO, Dy/Sm-BMO and Er/Nd-BMO samples under visible light.

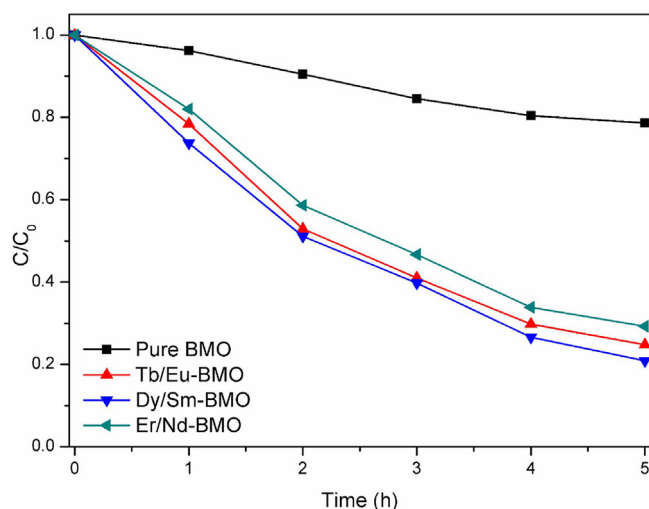


Fig. 7. Photocatalytic degradation of phenol (40 mL, 15 mg L⁻¹) over 0.04 g samples under 5 h of visible light irradiation.

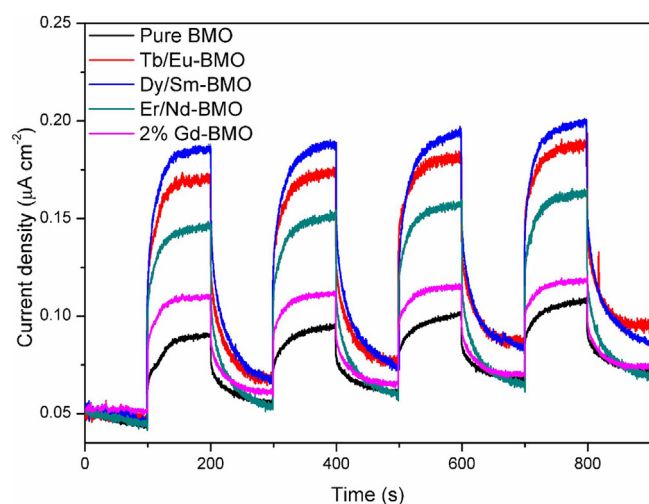


Fig. 8. Photocurrent responses of pure BMO, Tb/Eu-BMO, Dy/Sm-BMO, Er/Nd-BMO and 2% Gd-BMO under visible light.

the photocurrent responses of the pure BMO, Ln₁/Ln₂-BMO and 2% Gd-BMO samples with light on and off. It can be observed that all photocurrent responses of the co-doped BMO samples have been improved, and the order of their photocurrent intensities were Dy/Sm-BMO > Tb/Eu-BMO > Er/Nd-BMO > 2% Gd-BMO > pure BMO. Particularly, Dy/Sm-BMO exhibited the highest photocurrent response and the worst visible-light absorption. It reasonably implied that the separation of photo-generated electron–holes pairs was greatly facilitated by doping with Ln₁/Ln₂ redox couple.

The photodegradation for organics in aqueous solution comes from the active species such as hydroxyl radicals ($\cdot\text{OH}$), holes in the valence band (h^+) and superoxide radicals ($\cdot\text{O}_2^-$). To better explore the detailed mechanism of improved photocatalytic activity with the Ln₁/Ln₂ redox couple, trapping experiments were performed to confirm the dominated reactive species involved in the photocatalytic process. Three different quenchers isopropanol (IPA, 10 mM), sodium oxalate ($\text{Na}_2\text{C}_2\text{O}_4$, 10 mM) and benzoquinone (BQ, 1 mM) were used as hydroxyl radicals ($\cdot\text{OH}$), holes (h^+) and superoxide radicals ($\cdot\text{O}_2^-$) scavengers, respectively [51]. Fig. 9 reveals that both the photo-degradation ratios of RhB by Tb/Eu-BMO, Dy/Sm-BMO and Er/Nd BMO were almost not affected by the addition of IPA, indicating that $\cdot\text{OH}$ was not the main active species in the

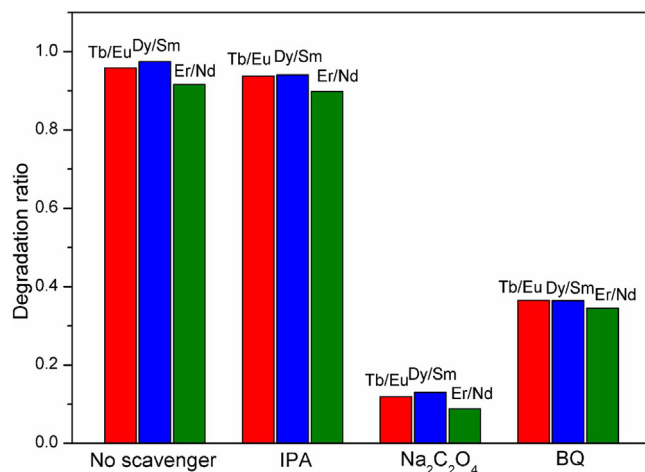


Fig. 9. Photocatalytic degradation ratio of RhB over the Tb/Eu-BMO, Dy/Sm-BMO and Er/Nd-BMO under visible light with adding scavengers IPA, $\text{Na}_2\text{C}_2\text{O}_4$ and BQ, respectively.

photocatalytic reaction process. By contrast, all the photocatalytic activities of Tb/Eu-BMO, Dy/Sm-BMO and Er/Nd-BMO were apparently restrained after adding $\text{Na}_2\text{C}_2\text{O}_4$ or BQ. The above results implied that the holes (h^+) and superoxide radicals ($\cdot\text{O}_2^-$) were the main active species in the degradation process of organics by Ln₁/Ln₂-BMO under visible light.

Based on the above analysis results, a conceivable mechanism for the enhanced photocatalytic activity of the Ln₁/Ln₂-BMO photocatalysts was proposed as illustrated in Fig. 10. It is well-known that a new doping level can be generated by doping with lanthanide ions, and the diverse theoretical which employed band calculations and cluster models have been made to describe the role of the 4f electrons in position 4f levels relative to the valence band [52]. Based on the analysis results of DRS, the guessable Ln₁/Ln₂ doping levels in BMO were located in 0.41 eV for Tb/Eu, 0.10 eV for Dy/Sm and 0.11 eV for Er/Nd co-doped level above the valence band of BMO, respectively. The result shows that Tb/Eu co-doping displayed the highest doping level, which could lead to the best photocatalytic activity in theory. However, Dy/Sm co-doping, which has the lowest doping level, exhibited the strongest photocatalytic activity and highest photocurrent intensity. Therefore, the main enhancement mechanism may be attributed to the improved charge separation efficiency, because the presence of the Ln₁/Ln₂ redox couple can facilitate charge transfer and suppress charge recombination in the BMO bulk. Just as illustrated in Fig. 10, the excited electrons in conduction band are captured by the Ln₁/Ln₂ redox couple, and then the trapped electrons can easily transfer to the oxygen molecules (O_2) adsorbed on the surface of the BMO photocatalysts. The trapping and releasing process of photo-induced electrons delayed the recombination rate of photo-generated electron–hole pairs, which contributed to the degradation of organics by the main reactive species of hole (h^+) and another reactive species superoxide radical ($\cdot\text{O}_2^-$). Thus, this above process can effectively enhance the activity of the photocatalysts.

However, why the Ln₁/Ln₂ redox couple possesses the ability of trapping and releasing photo-induced electrons, just as the photocatalytic mechanism of gadolinium in Bi_2WO_6 ? [53] A new conjecture about the complementary distribution of 4f orbital electrons in the Ln₁/Ln₂ redox couple was proposed as shown in Fig. 11. The 4f orbital of lanthanide ions can be divided into seven orbital, and respectively belong to $4f\sigma$, $4f\pi$, $4f\delta$, and $4f\phi$ orbitals [54]. It might be hard to confirm the nature of Ln₁ and Ln₂ interaction if both of the two Ln³⁺ centers have their own orbital momentum. Thus, this restricts our study to heterodinuclear couple including

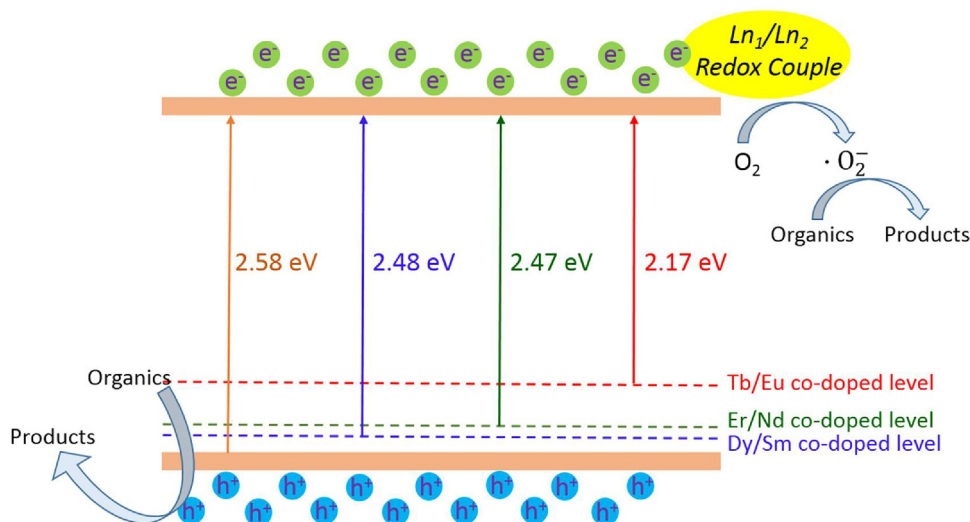


Fig. 10. Schematic illustration of the possible mechanism for the improved photocatalytic performance in Ln_1/Ln_2 -BMO.

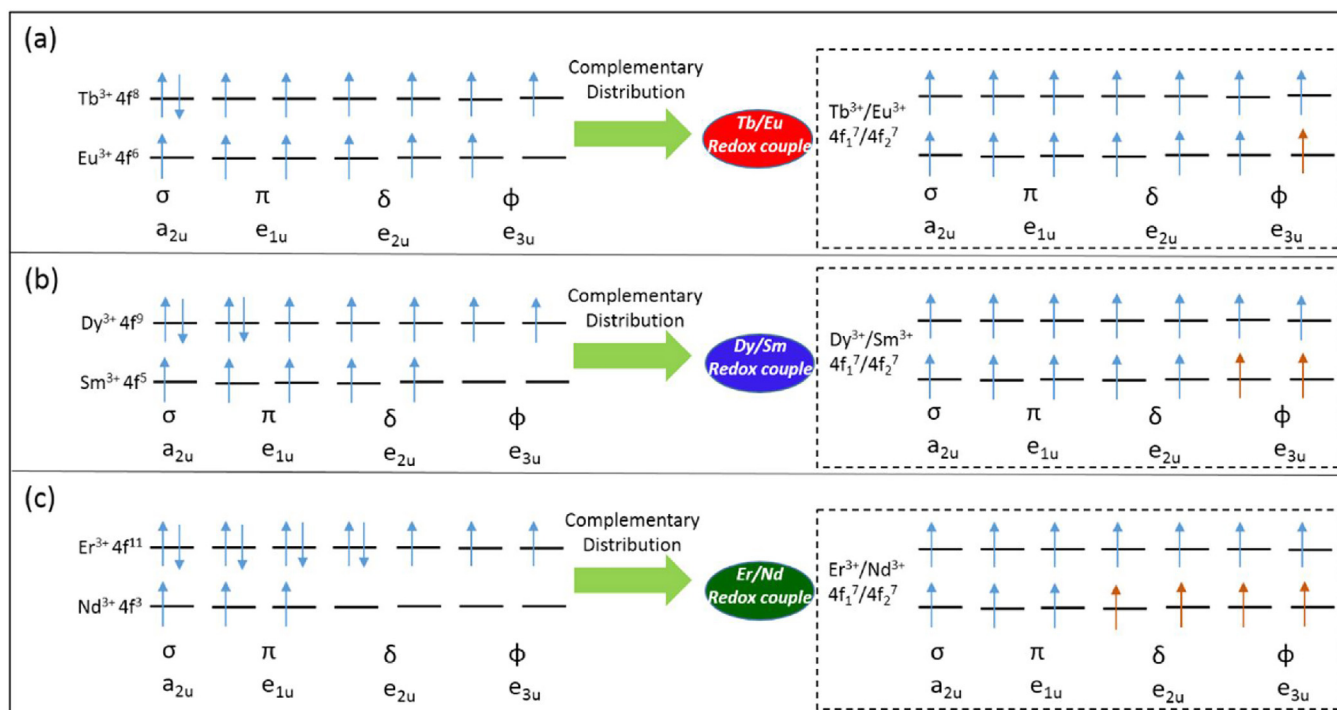


Fig. 11. Schematic representation of the complementary distribution of 4f orbital electrons in the (a) Tb/Eu redox couple, (b) Dy/Sm redox couple and (c) Er/Nd redox couple, respectively.

a Ln_1 ion and a Ln_2 ion which occupying an orbital momentum [55]. After co-doping with the same proportion of Ln_1 and Ln_2 ions in BMO, a plausible phenomenon would be occurred as follows: the redundant electrons of Ln_1 4f₁ orbital would be transferred to the unoccupied orbital of Ln_2 4f₂, then the coupling-half-filled in the 4f₁/4f₂ orbital that both holds 7 f-electrons were formed, and this configuration is relatively stable. Particularly, the similar complementary distribution was also occurred in multivalence lanthanide ion pairs, such as $\text{Tb}^{3+}/\text{Eu}^{3+}$ and $\text{Tb}^{4+}/\text{Eu}^{2+}$. In a word, it is because this coupling-half-filled in the 4f₁/4f₂ orbital is similar to the Gd^{3+} 4f orbital, the Ln_1/Ln_2 redox couple exhibits the ability of trapping and releasing electrons, which result in enhanced photocatalytic activity of BMO. Additionally, both the photocatalytic activities and photocurrent responses of Ln_1/Ln_2 -BMO were higher

than that of Gd -BMO (Figs. 6d and 8), which attributed to longer lasting electrons-transferring was occurred in heterodinuclear ions as comparison to that of mononuclear ions.

Predictably, the more different in number of 4f electrons between Ln_1 and Ln_2 ions, the poorer effect of the complementary distribution of 4f electrons. Among the three ions pairs co-doped BMO, Er/Nd -BMO displayed the weakest photocurrent response as well as the worst photocatalytic activity, which confirmed the above ideas. Nevertheless, it can be observed that both the photocurrent response and photocatalytic performance of Tb/Eu -BMO were lower than that of Dy/Sm -BMO, though their less different in number of 4f electrons between Tb and Eu ions. These findings give a reliable reference that the Ln_1/Ln_2 redox couple with appropriate difference in number of 4f electrons could have a significant influ-

ence on the separation of photoexcited carriers and light absorption in the photoreaction process.

4. Conclusions

In summary, the relevant $\text{Ln}_1^{3+} 4f^{7+x}/\text{Ln}_2^{3+} 4f^{7-x}$ ($\text{Ln}_1/\text{Ln}_2 = \text{Tb}/\text{Eu}$, Dy/Sm , Er/Nd ; $x = 1, 2, 4$) co-doped Bi_2MoO_6 (BMO) samples shows higher photocatalytic activities compared with other Ln_a/Ln_b co-doped or the corresponding single-doped samples. For all the three kinds of ions pairs co-doped BMO, the same proportion of Ln_1 and Ln_2 co-doped BMO (Ln_1/Ln_2 -BMO) display the highest photocatalytic activity. Both the photocatalytic activities and photocurrent responses of Ln_1/Ln_2 -BMO were higher than that of Gd^{3+} doped BMO, which attributed to longer lasting electrons-transferring was occurred in heterodinuclear ions as comparison to that of mononuclear ions. The heterodinuclear redox couple engineering by co-doping of Ln_1 and Ln_2 ions in BMO not only proposes a new conjecture about the complementary distribution between the $4f$ orbital electrons of Ln_1 and Ln_2 ions, but also provides a novel strategy to fabricate high-efficiency photocatalysts by selecting appropriate Ln_1/Ln_2 redox couple.

Acknowledgments

We gratefully acknowledge the financial support provided by the Project of the National Natural Science Foundation of China (Grant No. 21271022)

References

- [1] Q.J. Xiang, J.G. Yu, M. Jaroniec, *J. Am. Chem. Soc.* 134 (2012) 6575–6578.
- [2] A. Kubacka, M. Fernandez-Garcia, G. Colon, *Chem. Rev.* 112 (2011) 1555–1614.
- [3] C. Li, G. Chen, J. Sun, Y. Feng, J. Liu, H. Dong, *Appl. Catal. B: Environ.* 163 (2015) 415–423.
- [4] J. Chen, S. Shen, P. Wu, L. Guo, *Green Chem.* 17 (2015) 509–517.
- [5] D. Wu, S. Yue, W. Wang, T. An, G. Li, H.Y. Yip, H. Zhao, P.K. Wong, *Appl. Catal. B: Environ.* 192 (2016) 35–45.
- [6] C. Li, G. Chen, J. Sun, J. Rao, Z. Han, Y. Hu, W. Xing, C. Zhang, *Appl. Catal. B: Environ.* 188 (2016) 39–47.
- [7] K.M. Cho, K.H. Kim, H.O. Choi, H.T. Jung, *Green Chem.* 17 (2015) 3972–3978.
- [8] H. Li, Q. Deng, J. Liu, W. Hou, N. Du, R. Zhang, X. Tao, *Catal. Sci. Technol.* 4 (2014) 1028–1037.
- [9] N.T. Nguyen, M. Altomare, J.E. Yoo, N. Taccardi, P. Schmuki, *Adv. Energy Mater.* 6 (2016) 1501926.
- [10] J. Liu, Y. Yang, N. Liu, Y. Liu, H. Huang, Z. Kang, *Green Chem.* 16 (2014) 4559–4565.
- [11] D.H. Wang, L. Jia, X.L. Wu, L.Q. Lu, A.W. Xu, *Nanoscale* 4 (2012) 576–584.
- [12] K. Wang, Q. Li, B. Liu, B. Cheng, W. Ho, J. Yu, *Appl. Catal. B: Environ.* 176 (2015) 44–52.
- [13] D. Venieri, A. Fraggadakis, M. Kostadima, E. Chatzisympson, V. Binas, A. Zachopoulos, K. George, D. Mantzavinos, *Appl. Catal. B: Environ.* 154 (2014) 93–101.
- [14] S. Obregón, G. Colón, *Appl. Catal. B: Environ.* 158 (2014) 242–249.
- [15] J. Nowotny, M.A. Alim, T. Bak, M.A. Idris, M. Ionescu, K. Prince, M.Z. Sahdan, K. Sopian, M.A.M. Teridi, W. Sigmund, *Chem. Soc. Rev.* 44 (2015) 8424–8442.
- [16] S. Okunaka, H. Tokudome, R. Abe, *J. Mater. Chem. A* 3 (2015) 14794–14800.
- [17] Z. Dai, F. Qin, H. Zhao, J. Ding, Y. Liu, R. Chen, *ACS Catal.* 6 (2016) 3180–3192.
- [18] H. Li, W. Li, S. Gu, F. Wang, H. Zhou, *Catal. Sci. Technol.* 6 (2016) 3510–3519.
- [19] F. Wang, W. Li, S. Gu, H. Li, X. Wu, X. Liu, *J. Chem-Eur.* 22 (2016) 12859–12867.
- [20] R. Jaiswal, J. Bharambe, N. Patel, A. Dashora, D.C. Kothari, A. Miotello, *Appl. Catal. B: Environ.* 168 (2015) 333–341.
- [21] P. Yang, C. Lu, N. Hua, Y. Du, *Mater. Lett.* 57 (2002) 794–801.
- [22] J. Reszczyńska, T. Grzyb, J.W. Sobczak, W. Lisowski, M. Gazda, B. Ohtani, A. Zaleska, *Appl. Catal. B: Environ.* 163 (2015) 40–49.
- [23] S. Obregón, G. Colón, *Appl. Catal. B: Environ.* 152 (2014) 328–334.
- [24] W. Zhang, N. Yu, L. Zhang, K. Jiang, Y. Chen, Z. Chen, *Mater. Lett.* 163 (2016) 16–19.
- [25] H. Li, W. Li, S. Gu, F. Wang, H. Zhou, X. Liu, C. Ren, *RSC Adv.* 6 (2016) 48089–48098.
- [26] A.W. Xu, Y. Gao, H.Q. Liu, *J. Catal.* 207 (2002) 151–157.
- [27] H. Xu, C. Wu, H. Li, J. Chu, G. Sun, Y. Xu, Y. Yan, *Appl. Surf. Sci.* 256 (2009) 597–602.
- [28] R. Guo, L. Fang, W. Dong, F. Zheng, M. Shen, *J. Phys. Chem. C* 114 (2010) 21390–21396.
- [29] W. Zhou, Y. Zhou, S. Tang, *Mater. Lett.* 59 (2005) 3115–3118.
- [30] B. Han, J. Zhang, P. Li, J. Li, Y. Bian, H. Shi, *J. Electron. Mater.* 44 (2015) 1028–1033.
- [31] D. Zhou, H. Wang, X. Yao, L. Pang, *J. Am. Ceram. Soc.* 91 (2008) 3419–3422.
- [32] D. Chen, Q. Hao, Z. Wang, H. Ding, Y. Zhu, *CrystEngComm* 18 (2016) 1976–1986.
- [33] V.V. Lazenka, M. Lorenz, H. Modarresi, K. Brachwitz, P. Schwinkendorf, T. Böntgen, J. Vanacken, M. Ziese, M. Grundmann, V.V. Moshchakov, *J. Phys. D: Appl. Phys.* 46 (2013) 175006.
- [34] B.K. Rai, S.R. Mishra, V.V. Nguyen, J.P. Liu, *J. Alloy. Compd.* 550 (2013) 198–203.
- [35] J.S. Park, Y.J. Yoo, J.S. Hwang, J.H. Kang, B.W. Lee, Y.P. Lee, *J. Appl. Phys.* 115 (2014) 013904.
- [36] S. Gu, W. Li, F. Wang, H. Li, H. Zhou, *Catal. Sci. Technol.* 6 (2016) 1870–1881.
- [37] F. Mercier, C. Alliot, L. Bion, N. Thompat, P. Toulhoat, *J. Electron Spectrosc.* 150 (2006) 21–26.
- [38] K.G. Tshabalala, S.H. Cho, J.K. Park, S.S. Pitale, I.M. Nagpure, R.E. Kroon, H.C. Swart, O.M. Ntwaeaborwa, *J. Alloy. Compd.* 509 (2011) 10115–10120.
- [39] T.M. Pan, C.H. Lu, *Appl. Phys. Lett.* 99 (2011) 113509.
- [40] T.M. Pan, C.C. Huang, *Appl. Surf. Sci.* 256 (2010) 7186–7193.
- [41] X. Cui, Z. Liu, L. Lin, G. Jin, H. Wang, B. Xu, *J. Mater. Eng. Perform.* 24 (2015) 461–467.
- [42] J. Reszczyńska, T. Grzyb, J.W. Sobczak, W. Lisowski, M. Gazda, B. Ohtani, A. Zaleska, *Appl. Catal. B: Environ.* 163 (2015) 40–49.
- [43] D.M. Tobaldi, R.A.S. Ferreira, R.C. Pullar, M.P. Seabra, L.D. Carlos, J.A. Labrincha, *J. Mater. Chem. C* 3 (2015) 4970–4986.
- [44] Y. Luo, G. Tan, G. Dong, H. Ren, A. Xia, *Ceram. Int.* 41 (2015) 3259–3268.
- [45] C. Guo, J. Xu, S. Wang, L. Li, Y. Zhang, X. Li, *CrystEngComm* 14 (2012) 3602–3608.
- [46] P. Dumrongrojthanath, T. Thongtem, A. Phuruangrat, S. Thongtem, *Res. Chem. Intermediat.* 42 (2016) 5087–5097.
- [47] T. Zhou, J. Hu, J. Li, *Appl. Catal. B: Environ.* 110 (2011) 221–230.
- [48] A.A. Alemi, R. Kashfi, B. Shabani, *J. Mol. Catal. A: Chem.* 392 (2014) 290–298.
- [49] H. Li, W. Li, S. Gu, F. Wang, X. Liu, C. Ren, *Mol. Catal.* 433 (2017) 301–312.
- [50] H. Huang, X. Han, X. Li, S. Wang, P. Chu, Y. Zhang, *ACS Appl. Mater. Inter.* 7 (2015) 482–492.
- [51] P.Y. Kuang, J.R. Ran, Z.Q. Liu, H.J. Wang, N. Li, Y.Z. Su, Y.G. Jin, S.Z. Qiao, *J. Chem-Eur.* 21 (2015) 15360–15368.
- [52] A.H. Krumpel, E. Van Der Kolk, D. Zeelenberg, A.J.J. Bos, K.W. Krämer, P. Dorenbos, *J. Appl. Phys.* 104 (2008) 073505.
- [53] N. Tian, Y. Zhang, H. Huang, Y. He, Y. Guo, *J. Phys. Chem. C* 118 (2014) 15640–15648.
- [54] N. Hosoya, K. Yada, T. Masuda, E. Nakajo, S. Yabushita, A. Nakajima, *J. Phys. Chem. A* 118 (2014) 3051–3060.
- [55] J.P. Costes, F. Nicodème, *J. Chem-Eur.* 8 (2002) 3442–3447.